Scientia Iranica, Vol. 11, No. 4, pp 339–350

SCIENTIA
IRANICA

Full Navier-Stokes Computations of Supersonic Flows over a Body at High Angles of Attack and Investigation of Crossflow Separation

M. Pasandideh Fard* and M. Malek Jafarian[1]

In this paper, a three-dimensional code is developed to solve turbulent supersonic flows over a blunt-nose-cylinder at 32° and 44° angles of attack. The method used is an explicit finite-volume Runge-Kutta time stepping model for unsteady, three-dimensional, full, Navier-Stokes equations. This model can handle arbitrary geometries by using general coordinate transformations. The flowfields under consideration contain extensive regions of crossflow separation. The Reynolds shear stress terms are modeled algebraically with modifications to correct the turbulent length and velocity scales in separated regions. Calculations performed using the developed code require a computational memory accessible on most personal computers. Numerical results are in good agreement with experimental measurements. Comparisons of turbulent flow with graphical visualization by means of helicity revealed that the Runge-Kutta time stepping algorithm conserves symmetry at high angles of attack.

INTRODUCTION

Developing methods for simulation of flowfields around bodies at high angles of attack is a topic of high interest in the literature. This is because of the requirements of modern aircraft and missile performance for higher maneuverability and, thus, a trend toward flight at high angles of attack. Many current design problems, including the prediction of missile fin loads, the optimization of fighter-type aircraft engine inlets and the heat-shield design of maneuvering reentry vehicles, require detailed knowledge of high angle of attack flowfields. These flowfields are complex and typically contain extensive regions of three-dimensional crossflow separation. The extent of the crossflow separation and the resulting strength of the leeward-side vortex structure are typically small at low angles of attack; the separation grows as the angle of attack is increased. The flow patterns that a body-of-revolution experiences as it is pitched from a 0° to 90° angle of attack fall into four categories, which reflect the diminishing influence of the axial flow [1]. At moderate angles of attack ($\alpha \approx 10°$), the crossflow about the body begins to separate over the leeside generating symmetrical, counter-rotating vortices on the leeside. At high angles of attack and depending on a number of other factors, the vortices over the leeside may become asymmetric and, consequently, the body experiences a large side force and a yawing moment [2]. At higher angles of attack ($\alpha \approx 60°$), the aft-end of the body develops an unsteady von Karman shedding. As the angle of attack approaches 90° , the entire body length exhibits a time-dependent vortex shedding pattern [3].

A number of works in this area reported in the literature [4-10] showed that numerical simulations of flow around bodies at high angles of attack result in symmetric solutions, as long as algorithms, boundary and initial conditions and grids are perfectly symmetric. Degani et al. [11-13] showed that a fully three-dimensional asymmetric flow could only be achieved when perturbing the symmetric base flow by an asymmetrically disposed time-invariant disturbance. Otherwise, the flow would remain symmetric even in the case of high angle of attack, where experimental results showed the presence of asymmetry. Other investigators [14-16], however, obtained asymmetric flow solutions without imposing fixed asymmetric disturbances. They have argued that the numerical algorithms they used were able to reveal the true nature of the flows by bypassing the symmetric base

*. *Corresponding Author, Department of Mechanical Engineering, Ferdowsi University, P.O. Box 91755-1111, Mashad, I.R. Iran.*
1. *Department of Mechanical Engineering, Ferdowsi University, P.O. Box 91755-1111, Mashad, I.R. Iran.*

solution. In the authors' viewpoint, this argument is not correct. It is thought that the asymmetric flow observed in experiments is because the tip of a body, in reality, cannot be perfectly symmetric. In simulations, however, considering a perfect symmetric body is possible [17] and simulation of the flow around a symmetric body should result in a symmetric solution. For flow around a symmetric body, therefore, the source of asymmetric solutions should be attributed to numerical errors corresponding to the algorithm used.

Levy et al. [17] performed numerical simulations at high angles of attack for flow around slender bodies of revolution at subsonic speeds using four different numerical algorithms: A partially flux-split algorithm, the Beam and Warming algorithm in its original and diagonal forms, and an algorithm combining block and diagonal forms. Comparison of the results revealed that the diagonal algorithm fails to conserve symmetry at high angles of attack and a spurious asymmetry is developed. They found that every time an inversion was made, in any cross section, at any radial distance from the body, a small asymmetric error was introduced. The presence of that numerical error affects different flows in different ways. For low-angle-of-attack flows the error is similar in behavior to that of round-off error and it does not grow. For high-angle-of-attack flows, where instability mechanisms exist, the error is similar in behavior to that of a distribution of geometrical perturbations. The perturbations change their position between time steps and extend over the whole flowfield, as opposed to being located only on the body. As a result, the developed flowfield becomes asymmetric in the absence of a real geometrical perturbation, but the asymmetric pattern that emerges fails to conform to the pattern that is observed in experiments. The asymmetric solutions in the simulations are, in fact, the result of numerical errors [17].

Numerical simulations for flows around bodies have some difficulties, such as the existence of shock waves in the vicinity of the forebody, the separated boundary layers on the leeside with developing symmetric or asymmetric vortices and the formation of wake-like leeside flow at high angles of attack with supersonic speeds. The accuracy of the solutions depends on many factors, one of which being the highly stretched grids needed to resolve the extensive regions of separation.

Degani and Schiff [18] reported the results of a supersonic study designed to extend the thin-layer parabolized Navier-Stokes technique to treat flows over bodies at large angles of attack. They investigated the effects of the algebraic eddy-viscosity turbulence model. Baysal et al. [2] simulated three-dimensional laminar supersonic flows over a blunt-nose-cylinder at large angles of attack. They solved mass averaged Navier-Stokes equations by an approximately factored, upwind-biased, implicit, finite volume scheme.

In this paper, three-dimensional turbulence supersonic flows over a blunt-nose-cylinder at 32° and 44° angles of attack are simulated. This flowfield is dominated by large-scale, multiple vortices generated by the crossflow separation. The full Navier-Stokes equations are solved using finite volume and Runge-Kutta time stepping techniques. To accelerate solution convergence, local time stepping and an implicit residual averaging method are used. Although these techniques have been used in various flowfields, no report was found in the literature that used them for simulating three-dimensional flows over slender bodies at high angles of attack.

Only Siclari et al. [14] used the Runge-Kutta time stepping technique to simulate supersonic flows over a body with a conical shape at high angles of attack. However, they used a 2-D conical coordinate system to study the 3-D flowfield for a cone. In the results of their simulations, the vortices in the two sides of the body are not symmetric. On the other hand, as Levy et al. [17] stated, when conical restrictions were imposed for a three-dimensional flow, the solution became asymmetric. It seems that the conical approximation makes the crossflow susceptible to the absolute instability that leads to vortex asymmetry in the flow past a cone. As discussed above, this asymmetry should be ascribed to the numerical errors in their simulations. In this paper, therefore, an explicit finite-volume Runge-Kutta time stepping scheme is used, which is capable of simulating the full Navier-Stokes equations for unsteady turbulent flows. The results of this method are compared with the experimental measurements and the method examined with regard to flow symmetry around the body.

Flowfield solutions are obtained over the body at a Mach number of $M = 1.6$ and a Reynolds number of $\mathrm{Re}_L = 3.335 \times 10^6$. Since the flow over the body at high angles of attack has the potential to develop asymmetry, the full body grid is used here. Surface pressure, aerodynamic coefficients and wake regions in the leeside plane are calculated and compared with experimental measurements. The results show that the typical Runge-Kutta time stepping algorithm with full Navier-Stokes equations results in symmetric solutions at high angles of attack. All simulations for this paper were run on a Pentium 600 MHz computer with 512 MB RAM.

MATHEMATICAL FORMULATIONS AND GOVERNING EQUATIONS

The three-dimensional unsteady full Navier-Stocks equations without body forces or external heat transfer can be transformed to the arbitrary curvilinear space

ξ, η and ζ, while retaining strong conservation law form. The resulting transformed equations can be written in non-dimensional form as:

$$\frac{\partial \hat{q}}{\partial t} + \frac{\partial(\hat{E}_i - \hat{E}_\nu)}{\partial \xi} + \frac{\partial(\hat{F}_i - \hat{F}_\nu)}{\partial \eta} + \frac{\partial(\hat{G}_i - \hat{G}_\nu)}{\partial \zeta} = 0, \tag{1}$$

where the vectors $\hat{E}_i, \hat{F}_i$ and $\hat{G}_i$ are the inviscid terms and $\hat{E}_\nu, \hat{F}_\nu$ and $\hat{G}_\nu$ represent the viscous shear stress and heat flux terms. Flux vectors are defined as follows:

$$\hat{q} = J^{-1} \begin{bmatrix} \rho \\ \rho u \\ \rho \nu \\ \rho w \\ e \end{bmatrix},$$

$$\hat{E}_i = J^{-1} \begin{bmatrix} \rho U \\ \rho u U + \xi_x P \\ \rho \nu U + \xi_y P \\ \rho w U + \xi_z P \\ (e+P)U \end{bmatrix},$$

$$\hat{F}_i = J^{-1} \begin{bmatrix} \rho V \\ \rho u V + \eta_x P \\ \rho \nu V + \eta_y P \\ \rho w V + \eta_z P \\ (e+P)V \end{bmatrix},$$

$$\hat{G}_i = J^{-1} \begin{bmatrix} \rho W \\ \rho u W + \zeta_x P \\ \rho \nu W + \zeta_y P \\ \rho w W + \zeta_z P \\ (e+P)W \end{bmatrix},$$

$$\hat{E}_\nu = J^{-1} \begin{bmatrix} 0 \\ \xi_x \tau_{xx} + \xi_y \tau_{xy} + \xi_z \tau_{xz} \\ \xi_x \tau_{yx} + \xi_y \tau_{yy} + \xi_z \tau_{yz} \\ \xi_x \tau_{zx} + \xi_y \tau_{zy} + \xi_z \tau_{zz} \\ \xi_x \beta_x + \xi_y \beta_y + \xi_z \beta_z \end{bmatrix},$$

$$\hat{F}_\nu = J^{-1} \begin{bmatrix} 0 \\ \eta_x \tau_{xx} + \eta_y \tau_{xy} + \eta_z \tau_{xz} \\ \eta_x \tau_{yx} + \eta_y \tau_{yy} + \eta_z \tau_{yz} \\ \eta_x \tau_{zx} + \eta_y \tau_{zy} + \eta_z \tau_{zz} \\ \eta_x \beta_x + \eta_y \beta_y + \eta_z \beta_z \end{bmatrix},$$

$$\hat{G}_\nu = J^{-1} \begin{bmatrix} 0 \\ \zeta_x \tau_{xx} + \zeta_y \tau_{xy} + \zeta_z \tau_{xz} \\ \zeta_x \tau_{yx} + \zeta_y \tau_{yy} + \zeta_z \tau_{yz} \\ \zeta_x \tau_{zx} + \zeta_y \tau_{zy} + \zeta_z \tau_{zz} \\ \zeta_x \beta_x + \zeta_y \beta_y + \zeta_z \beta_z \end{bmatrix}, \tag{2}$$

where U, V and W are contravariant velocities written without metric normalization and u, ν and w are the non-dimensionalized Cartesian velocity components in the x, y and z directions, respectively. ρ is the density; P the pressure; and e the total energy. Total energy is related to the flow variables by the following perfect gas equation of state:

$$e = \frac{P}{\gamma - 1} + \frac{1}{2}\rho(u^2 + \nu^2 + w^2), \tag{3}$$

where γ is the ratio of specific heats. The shear stress terms like τ_{xx}, τ_{yy}, etc., metric coefficients like ξ_x, ξ_y, etc., contravariant velocities and β_x, β_y and β_z have been defined in [19].

NUMERICAL METHOD

Using:

$$\hat{E} = \hat{E}_i - \hat{E}_\nu, \quad \hat{F} = \hat{F}_i - \hat{F}_\nu, \quad \hat{G} = \hat{G}_i - \hat{G}_\nu, \tag{4}$$

and assuming J^{-1} to be independent of time, Equation 1 can be written as:

$$J^{-1} q_t + \hat{E}_\xi + \hat{F}_\eta + \hat{G}_\zeta = 0. \tag{5}$$

In a cell-centered finite-volume method, Equation 5 is integrated over a computational cell in the discretized computational domain and J^{-1} is identified as the cell volume. To advance the scheme in time, the multi-stage scheme is applied [20]. A typical step of a Runge-Kutta (4-stages) approximation to Equation 5 is:

$$q^{(k)} = q^{(0)} - \alpha_k \frac{\Delta t}{J^{-1}} \Big[D_\xi \hat{E}^{(k-1)} + D_\eta \hat{F}^{(k-1)} + D_\zeta \hat{G}^{(k-1)} + AD \Big]. \tag{6}$$

Assuming that:

$$R^{(k-1)} = D_\xi \hat{E}^{(k-1)} + D_\eta \hat{F}^{(k-1)} + D_\zeta \hat{G}^{(k-1)} - AD, \tag{7}$$

Equation 6 can be written as:

$$q^{(k)} = q^{(0)} - \alpha_k \frac{\Delta t}{J^{-1}} R^{(k-1)}, \tag{8}$$

where:

$$\alpha_k = \left(\frac{1}{4}, \frac{1}{3}, \frac{1}{2}, 1 \right),$$

and D_ξ, D_η and D_ζ are spatial differencing operators. The bracketed superscript in Equation 6 refers to the stages of the Runge-Kutta scheme and AD is the artificial dissipation term.

The basic elements of the scalar artificial dissipation model considered in this paper were first introduced by Jameson et al. [20], in conjunction with Runge-Kutta explicit schemes. This dissipation model has been used by many investigators [21] for numerical solution of the Euler and Navier-Stokes equations in a wide range of fluid dynamic applications. In Equation 6, AD is a combination of the second and fourth differences:

$$AD=\left(D_\xi^{(2)}+D_\eta^{(2)}+D_\zeta^{(2)}\ \ D_\xi^{(4)}\ \ D_\eta^{(4)}\ \ D_\zeta^{(4)}\right)q, \quad (9)$$

where, for example:

$$D_\xi^{(2)}q=\nabla_\xi\left[\left(\lambda_{i+\frac{1}{2},j,k}\ .\varepsilon^{(2)}_{i+\frac{1}{2},j,k}\right)\Delta_\xi\right]q_{ijk},$$

$$D_\xi^{(4)}q=\nabla_\xi\left[\left(\lambda_{i+\frac{1}{2},j,k}\ .\varepsilon^{(4)}_{i+\frac{1}{2},j,k}\right)\Delta_\xi\nabla_\xi\Delta_\xi\right]q_{ijk}. \quad (10)$$

The indices i,j and k are associated with the ξ,η and ζ directions, respectively and Δ_ξ and ∇_ξ are the standard forward and backward difference operators in the ξ direction. λ is a scaling factor, which will be defined later in this paper. The coefficients $\varepsilon^{(2)}_{i+\frac{1}{2},j,k}$ and $\varepsilon^{(4)}_{i+\frac{1}{2},j,k}$ are dissipation constants and are defined as:

$$\varepsilon^{(2)}_{i+\frac{1}{2},j,k}=\min\left(\frac{1}{2},\kappa^{(2)}\psi\right),$$

$$\varepsilon^{(4)}_{i+\frac{1}{2},j,k}=\max\left(0,\kappa^{(4)}\quad\alpha_{\text{diss}}\psi\right), \quad (11)$$

where:

$$\psi=\max\left(\nu_{i\ \ 1,j,k},\nu_{i,j,k},\nu_{i+1,j,k},\nu_{i+2,j,k}\right),$$

$$\nu_{i,j,k}=\left|\frac{\rho_{i+1,j,k}\quad 2\rho_{i,j,k}+\rho_{i\ \ 1,j,k}}{\rho_{i+1,j,k}+2\rho_{i,j,k}+\rho_{i\ \ 1,j,k}}\right|,$$

$$\kappa^{(2)}=1,\quad \kappa^{(4)}=\frac{1}{32},\quad \alpha_{\text{diss}}=2. \quad (12)$$

For the other directions, η and ζ, the contribution of dissipation is defined in a similar manner. The second-difference dissipation term is nonlinear; the purpose is to suppress oscillations in the neighborhood of shocks. This term is small in the smooth portion of the flowfield. The fourth-difference dissipation term is basically linear and is included to damp high-frequency modes and allow the scheme to approach a steady state condition; only this term affects the linear stability of the scheme and its value near shocks is reduced to zero [22].

Since the interest in this paper is only the steady flowfields, various techniques, like Local Time Stepping and Implicit Residual Averaging, are used to accelerate convergence.

The local time step is taken to be:

$$\Delta t_{ijk}=\frac{\text{CFL}.J^{\ \ 1}}{\overline{\lambda}_\xi+\overline{\lambda}_\eta+\overline{\lambda}_\zeta}, \quad (13)$$

where $\overline{\lambda}_\xi,\overline{\lambda}_\eta$ and $\overline{\lambda}_\zeta$ are average spectral radii of the flux Jacobian matrices in ξ,η and ζ directions, respectively:

$$\overline{\lambda}_\xi=\frac{1}{2}\left(\lambda_{i+\frac{1}{2},j,k}+\lambda_{i\ \ \frac{1}{2},j,k}\right),$$

$$\overline{\lambda}_\eta=\frac{1}{2}\left(\lambda_{i,j+\frac{1}{2},k}+\lambda_{i,j\ \ \frac{1}{2},k}\right),$$

$$\overline{\lambda}_\zeta=\frac{1}{2}\left(\lambda_{i,j,k+\frac{1}{2}}+\lambda_{i,j,k\ \ \frac{1}{2}}\right), \quad (14)$$

and:

$$\lambda_{i+\frac{1}{2},j,k}=\frac{1}{2}\left((\lambda_\xi)_{i,j,k}+(\lambda_\xi)_{i+1,j,k}\right),$$

$$\lambda_{i\ \ \frac{1}{2},j,k}=\frac{1}{2}\left((\lambda_\xi)_{i,j,k}+(\lambda_\xi)_{i\ \ 1,j,k}\right),$$

$$\lambda_{i,j+\frac{1}{2},k}=\frac{1}{2}\left((\lambda_\eta)_{i,j,k}+(\lambda_\eta)_{i,j+1,k}\right),$$

$$\lambda_{i,j\ \ \frac{1}{2},k}=\frac{1}{2}\left((\lambda_\eta)_{i,j,k}+(\lambda_\eta)_{i,j\ \ 1,k}\right),$$

$$\lambda_{i,j,k+\frac{1}{2}}=\frac{1}{2}\left((\lambda_\zeta)_{i,j,k}+(\lambda_\zeta)_{i,j,k+1}\right),$$

$$\lambda_{i,j,k\ \ \frac{1}{2}}=\frac{1}{2}\left((\lambda_\zeta)_{i,j,k}+(\lambda_\zeta)_{i,j,k\ \ 1}\right). \quad (15)$$

The scaled spectral radii of the flux Jacobian matrices for the convective terms are:

$$\lambda_\xi=|U|+c\sqrt{\xi_x^2+\xi_y^2+\xi_z^2},$$

$$\lambda_\eta=|V|+c\sqrt{\eta_x^2+\eta_y^2+\eta_z^2},$$

$$\lambda_\zeta=|W|+c\sqrt{\zeta_x^2+\zeta_y^2+\zeta_z^2}, \quad (16)$$

where c is the speed of sound.

The implicit residual averaging technique is used to extend the stability limit and the robustness of the basic scheme. In three dimensions, the residual is handled as follows:

$$(1\ \ \chi\nabla_\xi\Delta_\xi)(1\ \ \chi\nabla_\eta\Delta_\eta)(1\ \ \chi\nabla_\zeta\Delta_\zeta)\overline{R}_{ijk}=R_{ijk}, \quad (17)$$

where $\overline{R}_{ijk}$ is the average residual. The constant χ may have typical values ranging from 0.1 to 0.5. The residual averaging requires three tridiagonal inversions, which is computationally time consuming. The residual averaging is applied to every stage of the Runge-Kutta scheme in this paper.

TURBULENCE MODEL

The simulation of turbulent crossflow separation about slender bodies at high angles of attack poses numerical difficulties. Most turbulence models are validated by comparison with 2-D and axisymmetric flows. The extension of these models to 3-D flows with significant adverse pressure gradients, separated shear layers and strong vortices outside the boundary layer, is challenging. Many researchers in this field have proposed "fixes" for the Baldwin-Lomax algebraic turbulence model [23], in order to determine the correct boundary layer length scale in the presence of separated free shear layers [18,24]. Murman and Chaderjian [25] examined similar fixes for the Spalart-Allmaras one-equation model. Neither of these efforts could provide results of the same accuracy as obtained using the Degani-Schiff [18] corrections to the Baldwin-Lomax model. This model, therefore, is used in this paper to calculate the local values of the eddy viscosity. In the two-layer model, μ_t is given by:

$$\mu_t = \min(\mu_i, \mu_o), \tag{18}$$

where:

$$\mu_i = \rho l^2 |\omega|, \quad \mu_o = \rho K C_{cp} F_{\text{wake}} F_{\text{kleb}}(y). \tag{19}$$

K and C_{cp} are constant; l is the length scale; $|\omega|$ is the local vorticity; and $F_{\text{kleb}}(y)$ is the Klebanoff intermittency factor. Thus, one has:

$$l = ky\left(1 \quad \exp\left(\frac{y^+}{A^+}\right)\right),$$

$$\omega = \sqrt{(u_y \quad \nu_x)^2 + (\nu_z \quad w_y)^2 + (w_x \quad u_z)^2},$$

$$F_{\text{wake}} = y_{\max} F_{\max},$$

$$F_{\text{kleb}}(y) = \left(1 + 5.5\left(\frac{C_{\text{kleb}}\, y}{y_{\max}}\right)^6\right)^{\ \ 1}, \tag{20}$$

where k, A^+ and C_{kleb} are constants and $F_{\max}$ is the maximum value of the function $F(y)$ defined with y^+ as follows:

$$y^+ = y\frac{\sqrt{\rho_w \tau_w}}{\mu_w}, \quad F(y) = y|\omega|\left(1 \quad \exp\left(\frac{y^+}{A^+}\right)\right), \tag{21}$$

$y_{\max}$ is the value of y at which $F_{\max}$ occurs. The constants appearing in Equations 19 and 20 were determined to be:

$$A^+ = 26,\ k = 0.4,\ K = 0.0168,\ C_{cp} = 1.6,\ C_{\text{kleb}} = 0.3.$$

The major difficulty in applying the Baldwin-Lomax turbulence model to bodies with crossflow separation is proper evaluation of the scale length, $y_{\max}$, and, in turn, correct calculation of μ_o for boundary layer profiles in the crossflow separation region. On the windward side at $\phi = \phi_1$ (Figure 1), the attached boundary layer gives rise to a profile of $F(y)$, which has a single, well-defined peak, as shown in Figure 2a. Thus, the determination of $F_{\text{wake}}(\phi_1)$ is straightforward. However, on the leeward side ray at $\phi = \phi_2$ (Figure 1), in addition to a local peak in $F(y)$ in the attached boundary layer at $y_2 = a$, the overlying vortex structure causes a larger peak in $F(y)$ at $y_2 = b$ (Figure 2b). The choice of the peak at $y_2 = b$ results in a high value of the outer layer eddy viscosity coefficient, μ_o. Therefore, in general, the calculated eddy viscosity coefficient in the crossflow separation region will be high; this will cause the details of the simulated flow to be distorted or washed out. To eliminate these difficulties, the first peak in $F(y)$ should be selected [18].

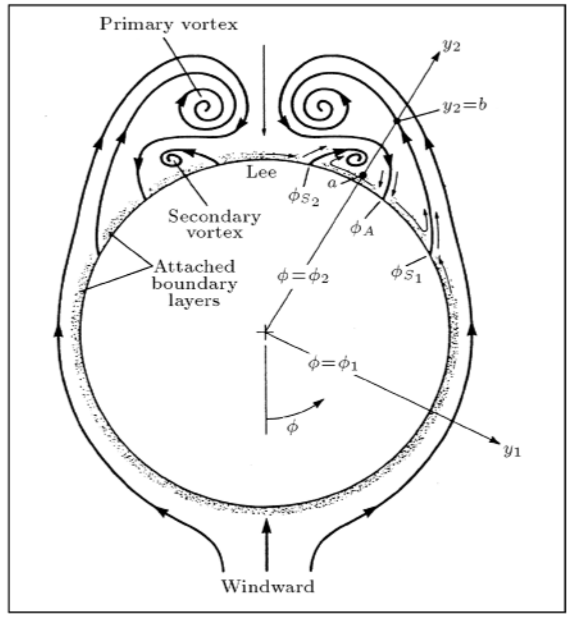

Figure 1. Flow structure in the crossflow plane [18].

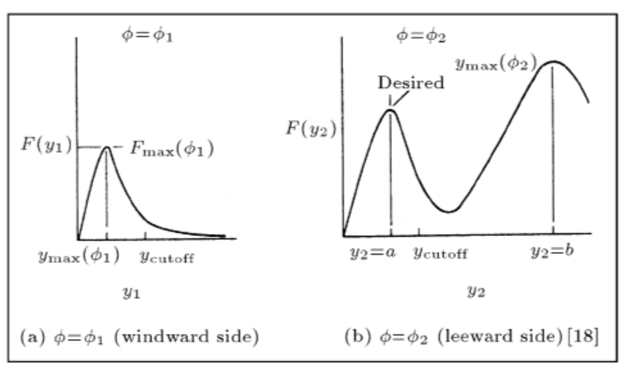

Figure 2. Behavior of $F(y)$ at larger incidence.

MODEL GEOMETRY AND COMPUTATIONAL GRID

To provide a basis for comparison, simulations about a blunt-nose-cylinder were run using the developed code by implementing the described explicit algorithm. This model geometry, shown in Figure 3, is the same as that used by Baysal et al. [2].

The C-O type grid used in this study was obtained from a grid generator, by first solving the two-dimensional Poisson's equations for half of the symmetry plane of the cylinder (x-y plane) and then rotating this grid about the axis of the cylinder (Figure 4). This program allows arbitrary grid point clustering, thus, enabling the grid points of the body shapes to be clustered in the vicinity of the body surface to resolve the viscous boundary layer. The results were obtained for a wide range of grid resolutions. The computational mesh had $60 \times 50 \times 120$ cells in the axial, radial, and circumferential directions, respectively. The minimum normal spacing was in the order of $10\ ^{4} \times D$.

RESULTS AND DISCUSSION

In order to validate the model, simulations were run under flow conditions, for which the experimental results were available [26]. In the simulations, two angles of attack of $\alpha = 32°$ and $\alpha = 44°$, a Mach number of $M_\infty = 1.6$ and a Reynolds number of $\mathrm{Re}_L = 3.335 \times 10^6$, with fully turbulent conditions, were considered.

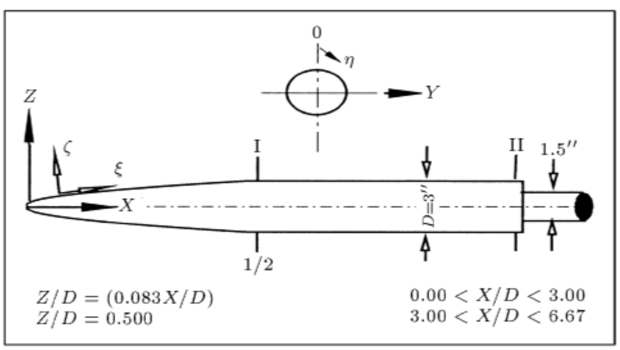

Figure 3. The schematic of the blunt-nose-cylinder [2].

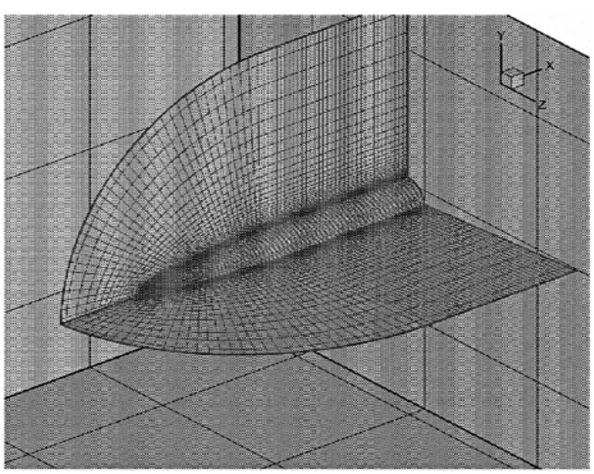

Figure 4. A representation of the grid section.

For the initial conditions, a uniform free stream flow was used all over the computational domain. On the body surface, no slip boundary conditions were used where $u = \nu = w = 0$ were set. The pressure and density were extrapolated at the body surface from the first grid line above the body surface. There were two outer boundaries: Inlet and downstream. At an inlet boundary, constant free stream values were assumed for all variables, whereas at a downstream boundary, all variables were obtained through extrapolation.

In order to study the issue of the flow asymmetry, the computations need to be done for the full body (with no symmetric plane) at an angle of attack higher than 30°. Therefore, for both cases ($\alpha = 32°$ and $\alpha = 44°$), the angle of attack was higher than 30° and calculations were performed about the full body ($\eta = 0 \quad 360°$).

The developed code needs a computer memory accessible on most personal computers. All the simulations were run on a Pentium 600 MHz computer with 512 MB RAM. A typical CPU time was around 63 hours where the computational rate (CPU time per iteration per cell) was around 100 μs.

Turbulent Flow at $\alpha = 32°$

The surface pressure coefficient is shown as a function of the longitudinal position for both the leeside and the windside in Figures 5a and 5b, respectively. As seen in these figures, there is a good agreement between calculated and measured values. From the calculations, the normal force coefficient (C_N) at an angle of attack of 32° is 4.185, which is in close agreement with the measured value of 4.190. When computing force coefficients, the base of the body was used as the reference area.

Figure 6 shows the calculated density contours over the body in the windside and leeside planes. The strong shock in the windside plane and the expansion waves in the leeside plane are seen clearly in this figure.

Two axial positions were selected to analyze the crossflow. The two positions, I and II in Figure 3, are located immediately after the forebody-cylinder junction ($X/D = 3.17$) and upstream of the base ($X/D = 6.17$), respectively. Crossflow density contours at positions I and II are shown in Figure 7. The presence of a lower density in each of the vortex cores identifies the primary and secondary vortices. The comparison shows that the strength of the primary vortices grows with increased distance downstream from the nose.

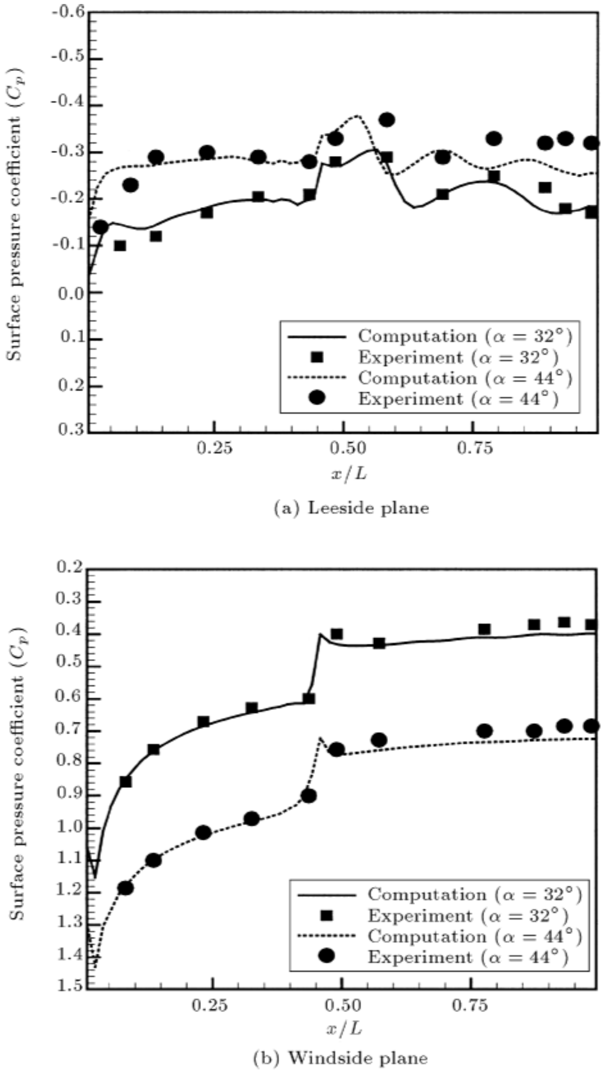

(a) Leeside plane

(b) Windside plane

Figure 5. Comparison of the calculated and measured longitudinal Cp distribution for $\alpha = 32°$ and $\alpha = 44°$ angles of attack.

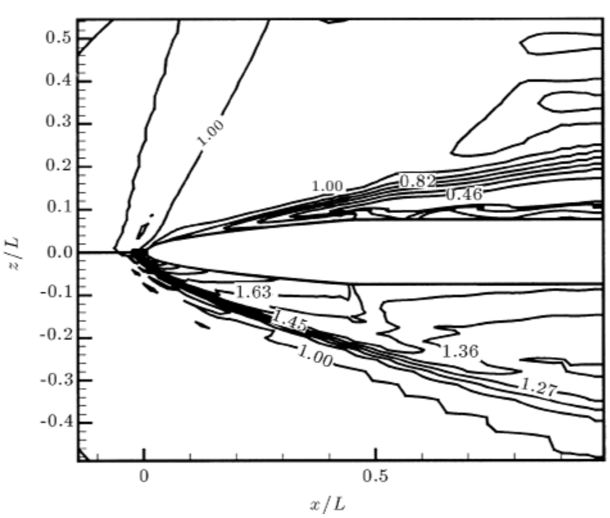

Figure 6. Calculated density contours at the symmetry plane for $\alpha = 32°$.

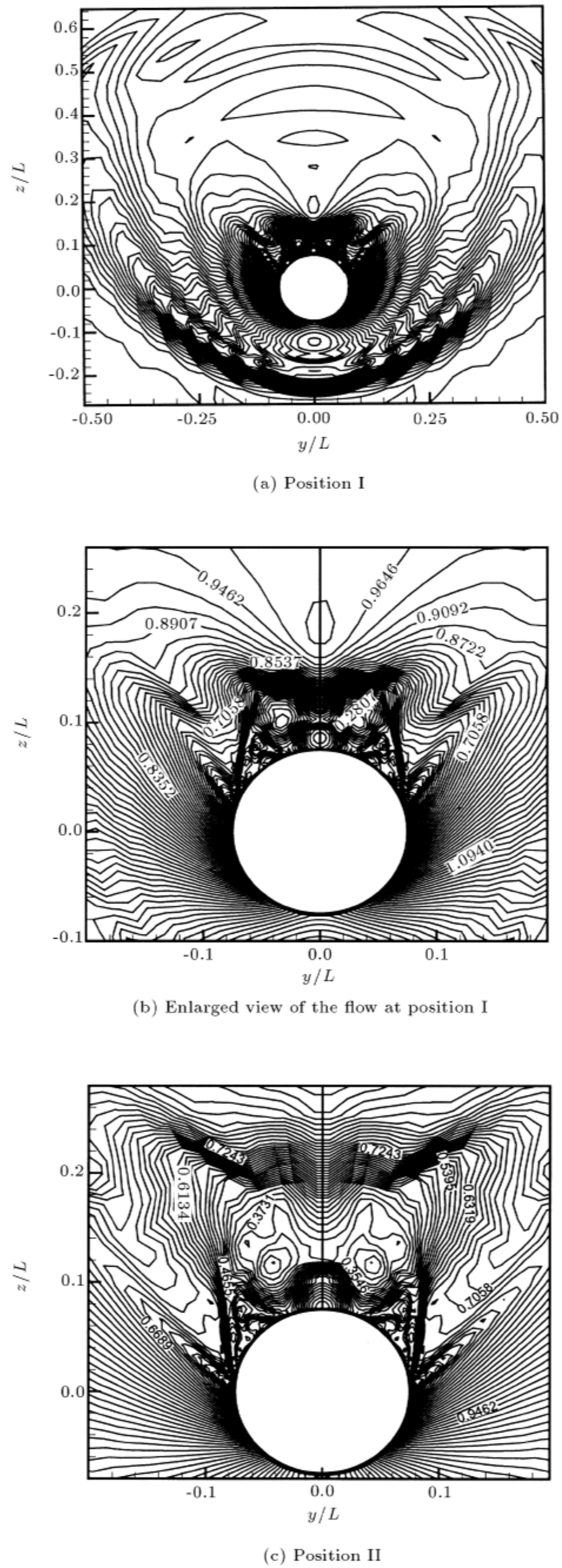

(a) Position I

(b) Enlarged view of the flow at position I

(c) Position II

Figure 7. Calculated crossflow density contours for $\alpha = 32°$.

The distribution of the circumferential skin friction coefficient (C_f) at position II (Figure 8) indicates that the primary separation occurs around $\eta = 275°$. This induced flow leaves the surface at a secondary separation point through a weak crossflow shock around $\eta = 328°$, with the fluid rolling up to form a secondary vortex and reattaching around $\eta = 303°$. The primary reattachment is about $\eta = 360°$.

Pressure or density plots can identify the cores of concentrated primary vortices in high-speed flows. These plots, however, are not sufficiently sensitive to identify low-speed flows, such as secondary vortices. As a result, they should not be used to differentiate between primary and secondary vortices. In addition, pressure or density plots do not give any information regarding the swirl direction of the vortices. As shown by Degani [27], the helicity density, a scalar quantity derived from the velocity, should be used instead. A helicity density plot can be used to identify the vortices and differentiate between primary and secondary vortices and indicate the direction of the swirling motion. Helicity density is defined as:

$$H_d = \vec{V}.\vec{\omega}.$$

The main advantage of helicity density over other scalar quantities is that both its magnitude and sign are meaningful. High values of helicity density reflect high values of speed and vorticity when the relative angle between them is small. The sign of the helicity density indicates the direction of swirl of the vortex relative to the streamwise velocity component.

Figure 9 shows the calculated helicity density contours at the two positions I and II. The angle between the velocity and vorticity vectors in the vortex-core region is small. This means that the helicity density, which is the cosine of this angle, will reach its highest absolute number in this region. This fact is

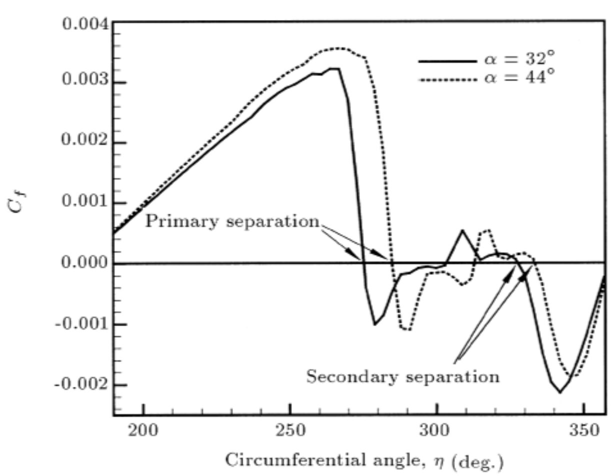

Figure 8. Circumferential skin friction distribution at position II for $\alpha = 32°$ and $\alpha = 44°$.

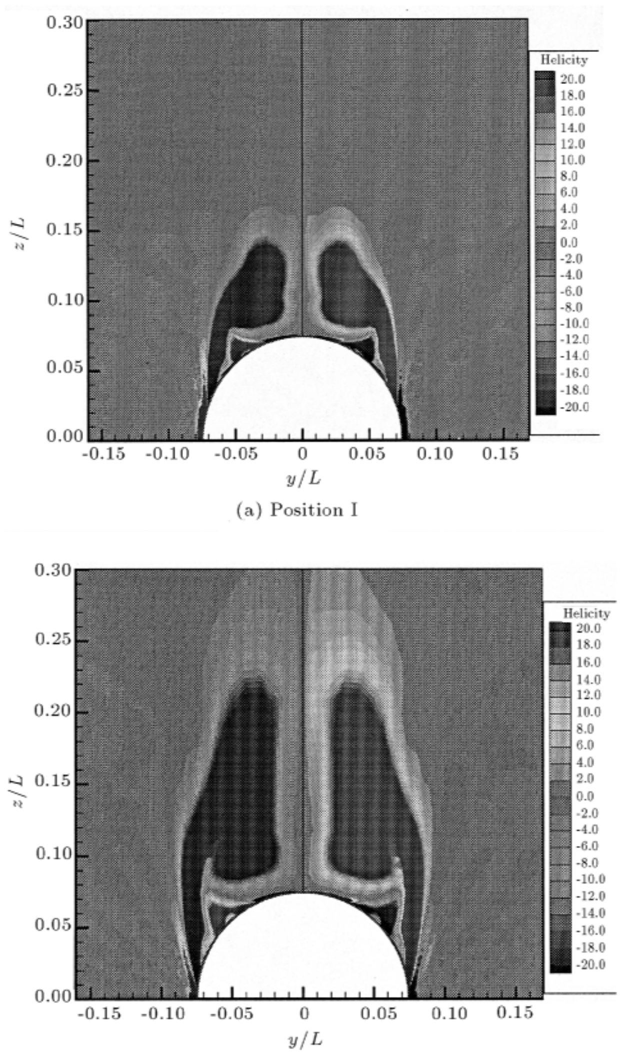

(a) Position I

(b) Position II

Figure 9. Calculated helicity density contours for $\alpha = 32°$.

used to locate the vortex axis. The obtained solution, shown in Figure 9, is completely symmetric, demonstrating that the computational procedure used can produce symmetric solutions on a full plane grid. The delineation of the vortices in this method is more visible than in the density contours (Figure 7). All vortices can be seen and the change in sign of the helicity density (the corresponding color) clearly distinguishes between primary and secondary vortices. The helicity density changes sign across every separation or reattachment line. The transition between the primary and secondary vortices, as well as the transition between the attached and separated flows, is visible in Figure 9.

The calculated circumferential surface pressure coefficient at position II, shown in Figure 10, confirms that the flowfield is symmetric close to the body surface, as well as in the wake.

The circumferential streamline patterns, shown in Figure 11, correspond to the two positions I and

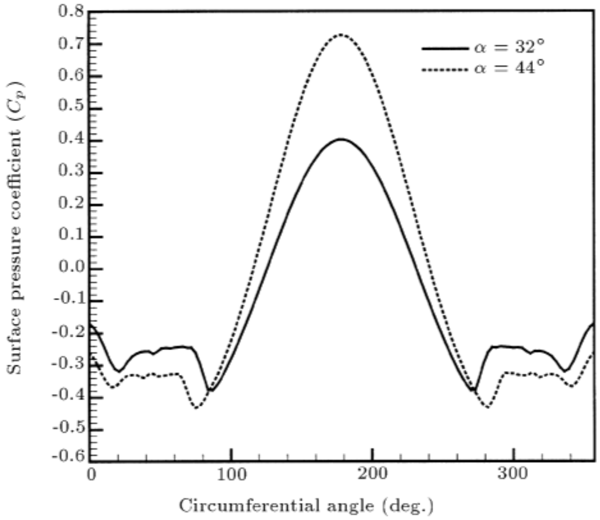

Figure 10. Calculated circumferential surface pressure distribution at position II for $\alpha = 32°$ and $\alpha = 44°$.

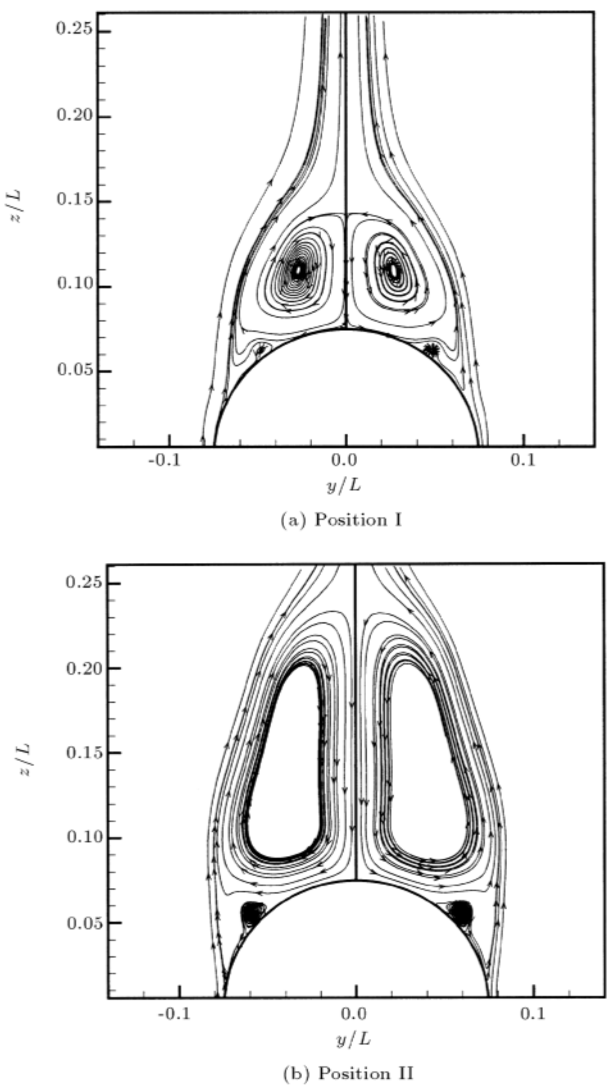

Figure 11. Calculated crossflow streamline patterns for $\alpha = 32°$.

II, respectively. As seen in the figure, the solution is symmetric and two separated vortices occur on each side of the leeside plane. The symmetric solution extends to the end of the body (position II) with qualitatively similar features; the vortices, however, are becoming larger relative to the diameter of the body.

Turbulent Flow at $\alpha = 44°$

Figures 5a and 5b show a good agreement between the calculated and measured longitudinal C_p distributions on the body for the leeside and windside planes. The calculated and measured values for C_N are 6.384 and 6.380, respectively.

Figure 8 shows the circumferential C_f distribution of the body at position II. The primary separation occurs around $\eta = 288°$ and the primary reattachment around $\eta = 360°$. The secondary separation and reattachment are seen to be around $\eta = 333.5°$ and $\eta = 313°$, respectively. Compared to the $\alpha = 32°$ case, the magnitude of C_f for the $\alpha = 44°$ case is larger everywhere, except in the secondary vortex region. Higher angle of attack is more resistant to separation, consequently, the secondary vortex is weaker.

Figures 12 and 13 show the density contours of the symmetry plane and crossflow density contours at the two positions I and II, respectively. As observed earlier, the strength of the primary vortices grow with increasing the distance downstream from the body.

A comparison between Figures 7 and 13 show that the strength of the vortices grows with increasing the angle of attack; this is because of the diminishing influence of the axial flow.

The calculated helicity density contours at the two positions I and II are given in Figure 14. Both the magnitude of the helicity density and the swirl

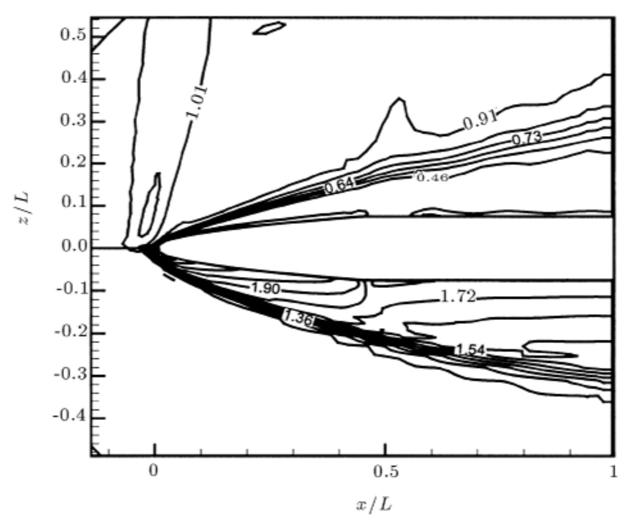

Figure 12. Calculated density contours at the symmetry plane for $\alpha = 44°$.

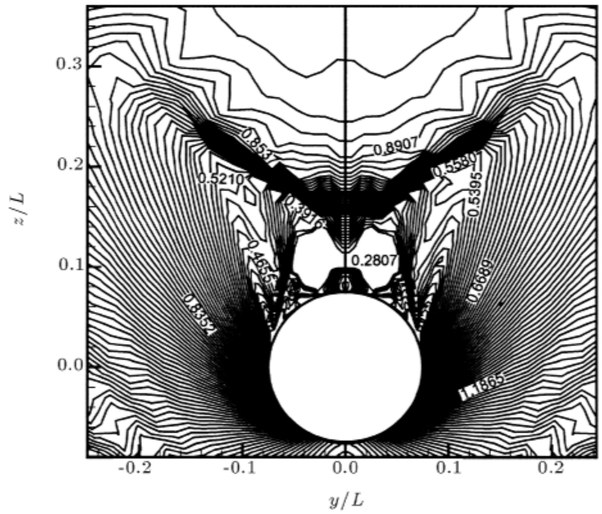

(a) Position I

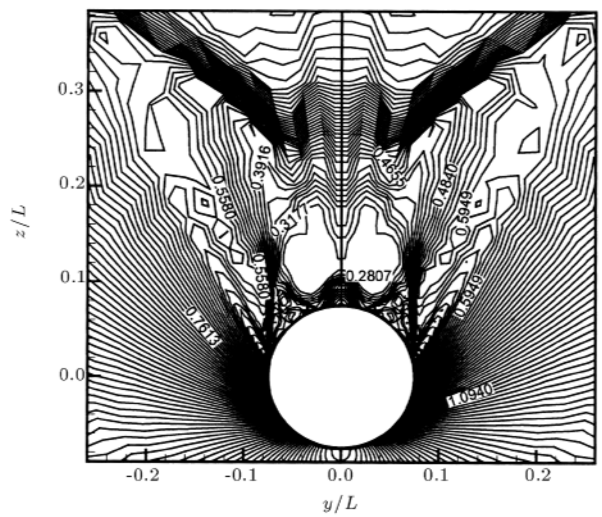

(b) Position II

Figure 13. Calculated crossflow density contours for $\alpha = 44°$.

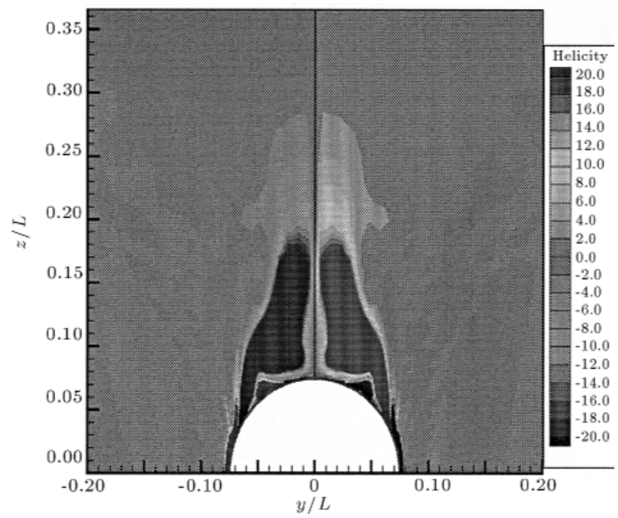

(a) Position I

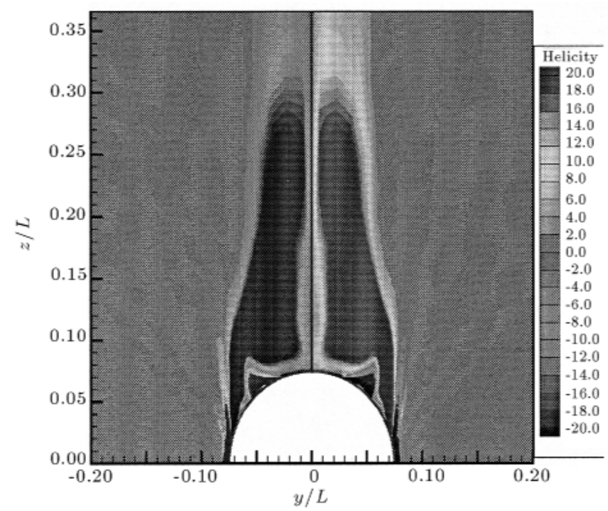

(b) Position II

Figure 14. Calculated helicity density contours for $\alpha = 44°$.

direction, shown by gradual change in color for magnitude and different colors for positive or negative directions, clearly distinguish primary and secondary vortices from each other. This figure shows perfect symmetry in the strength of the primary and secondary vortices and in the location of the primary and secondary separation lines. This confirms the symmetry of the flow at this angle of attack.

The crossflow streamline patterns shown in Figure 15 ($\alpha = 44°$) are similar to those of Figure 11 ($\alpha = 32°$); the symmetric solution for both cases extends to the end of the body.

CONCLUSIONS

An unsteady full Navier-Stokes code was developed to solve the three-dimensional vortical supersonic flows over a blunt-nose-cylinder at high angles of attack. Solutions were obtained using computationally efficient techniques. The modified Baldwin-Lomax turbulence model [18] was used to simulate turbulence crossflow separation. The calculated flowfield results were in good agreement with the experimental data reported in literature. It was shown that the strength of the primary vortices grows with increasing the distance downstream from the nose. In addition, the graphical visualization of vortical flows by means of helicity showed no asymmetric vortices on a full plane grid for $\alpha = 32°$ and $44°$; therefore, the calculated solution was symmetric. It was observed that the higher angle of attack is more resistant to flow separation and the strength of the vortices grows with increasing the angle of attack. The results showed that the popular Runge-Kutta time stepping algorithm with full Navier-Stokes equations results in symmetric solutions at high angles of attack.

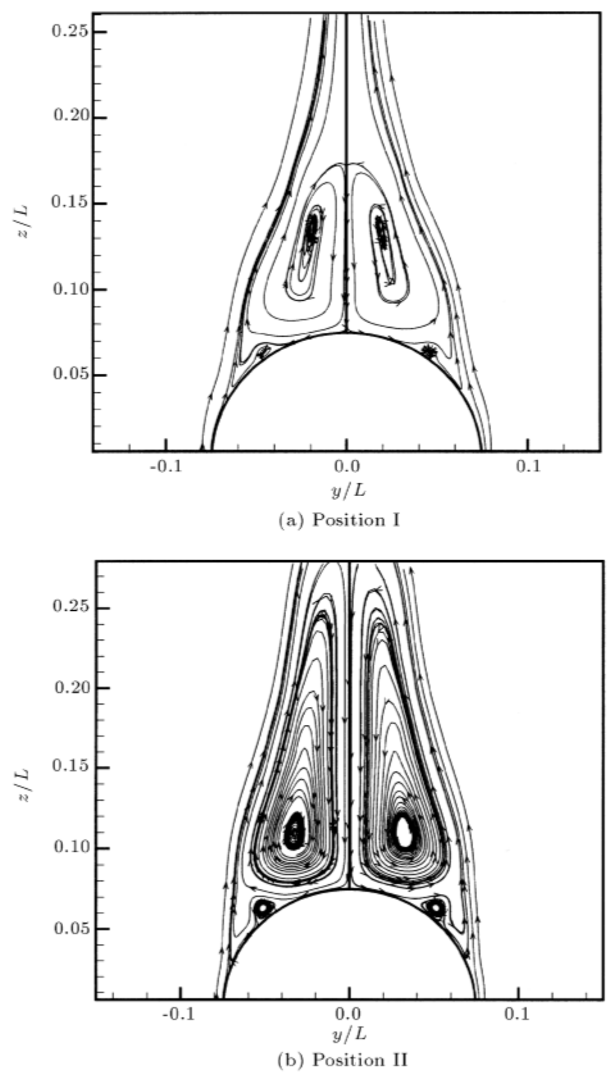

Figure 15. Calculated crossflow streamline patterns for $\alpha = 44°$.

ACKNOWLEDGMENT

This work was supported by the Ministry of Science, Research and Technology under national project No. 4698.

NOMENCLATURE

A^+	constant in turbulence model
AD	artificial dissipation
c	speed of sound
CFL	Courant-Friedrich-Lewy number
C_{cp}	constant in turbulence model
C_f	skin friction coefficient
C_{kleb}	constant in turbulence model
C_N	normal force coefficient
C_p	pressure coefficient
C_{wake}	constant in turbulence model
D	diameter of the body
D_ξ, D_η, D_ζ	spatial differencing operators
e	total energy
$\hat{E}_i, \hat{F}_i, \hat{G}_i$	inviscid flux vectors
$\hat{E}_\nu, \hat{F}_\nu, \hat{G}_\nu$	viscous flux vectors
F	function in turbulence model
F_{kleb}	Klebanoff factor in turbulence model
F_{wake}	wake function in turbulence model
H_d	helicity density
J^{-1}	Jacobian inverse of the coordinate transformation
K	constant in turbulence model
k	Von Karman constant in turbulence model
L	body length
l	length scale in turbulence model
M_∞	freestream Mach number
P	pressure
q	state vector
R	residual
Re_L	Reynolds number based on length of the body
U, V, W	contravariant velocity components
u, ν, w	Cartesian velocity components
x, y, z	Cartesian coordinate
y^+	non-dimensional distance from the wall
α	angle of attack
α_{diss}	constant in artificial dissipation scheme
α_k	constant in multistage scheme
γ	ratio of the specific heat
Δ_ξ	forward difference operation
Δt	time step size
$\varepsilon^{(2)}, \varepsilon^{(4)}$	dissipation constants
$\kappa^{(2)}, \kappa^{(4)}$	constants in artificial dissipation scheme
$\lambda_\xi, \lambda_\eta, \lambda_\zeta$	scaled spectral radii of the flux Jacobian matrices
μ_i, μ_o	inner and outer turbulence viscosity
μ_t	turbulence viscosity
ξ, η, ζ	curvilinear coordinates
ρ	density
τ	shear stress term
χ	constant in residual averaging technique
ω	vorticity
∇_ξ	backward difference operation

REFERENCES

1. Chapman, G.T. and Keener, E.R. "The aerodynamics of bodies of revolution at angles of attack", *AIAA Journal*, pp 79-0023 (Jan. 1979).
2. Baysal, O., Fouladi, K. and Miller, D.S. "Computations of supersonic flows over a body at high angle of attack", *AIAA Journal*, **27**(4), pp 427-437 (April 1989).
3. Murman, S.M. "Geometric perturbations and asymmetric vortex shedding about slender pointed bodies", *AIAA Journal*, pp 2000-4103-CP.
4. Allen, H.J. and Perkins, E.W. "A study of effects of viscosity on flow over slender inclined bodies of revolution", *NACA Rep.*, p 1048 (1951).
5. Thomson, K.D. and Morrison, D.F. "The spacing, position and strength of vortices in the wake of slender cylindrical bodies at large incidence", *Journal of Fluid Mechanics*, **50**, pp 751-783 (Dec. 1971).
6. Hunt, B.L. and Dexter, P.C. "Pressure on a slender body at high angle of attack in a very low turbulence level airstream", *AGARD CP 277*, p 17 (1978).
7. Dexter, P.C. and Hunt, B.L. "The effect of roll angle on the flow over a slender body of revolution at high angles of attack", *AIAA Journal*, pp 81-0358 (Jan. 1981).
8. Hunt, B.L. "Asymmetric vortex forces and wakes on slender bodies", *AIAA Journal*, pp 82-1336 (Aug. 1982).
9. Lamont, P.J. "Pressure around an inclined ogive cylinder with laminar, transitional or turbulent separation", *AIAA Journal*, **20**(5), pp 1492-1499 (1982).
10. Zilliac, G.G., Degani, D. and Tobak, M. "Asymmetric vortices on a slender body of revolution", *AIAA Journal*, **29**, pp 667-675 (1991).
11. Degani, D. "Effect of geometrical disturbance on vortex asymmetry", *AIAA Journal*, **29**(4), pp 560-566 (1991).
12. Degani, D. "Numerical investigation of the origin of vortex asymmetry", *AIAA Journal*, pp 90-0593 (Jan. 1990).
13. Degani, D. and Schiff, L.B. "Numerical simulation of the effect of spatial disturbances on vortex asymmetry", *AIAA Journal*, **29**(3), pp 344-352 (1991).
14. Siclari, M.J. and Marconi, F. "The computation of Navier-Stokes solutions exhibiting asymmetric vortices", *AIAA Journal*, pp 89-1817 (June 1989).
15. Kandil, O.A., Wong, T.C. and Lin, C.H. "Navier-Stokes computations of symmetric and asymmetric vortex shedding around slender bodies", *AIAA Journal*, pp 89-3397 (Aug. 1989).
16. Hartwich, P.M., Hall, R.M. and Hemsch, M.J. "Navier-Stokes computations of vortex asymmetries controlled by small surface imperfection", *AIAA Journal*, pp 90-0385 (Jan. 1990).
17. Levy, Y., Hesselink, L. and Degani, D. "Anomalous asymmetries in flows generated by algorithms that fail to conserve symmetry", *AIAA Journal*, **33**(6), pp 999-1007 (June 1995).
18. Degani, D. and Schiff, L.B. "Computation of turbulent supersonic flow around pointed bodies having crossflow separation", *J. Comp. Phys.*, **66**, pp 173-196 (1986).
19. Pulliam, T.H. and Steger, J.L. "Implicit finite-difference simulations of three-dimensional compressible flow", *AIAA Journal*, **18**(2), pp 159-167 (1980).
20. Jameson, A. and Schmidt, W. "Numerical solution of the euler equations by finite volume methods using Runge-Kutta time-stepping schemes", *AIAA Journal*, pp 81-1259 (June 1981).
21. Jameson, A. "The present status, challenges and future developments in computational fluid dynamics", *Twelfth Australasian Fluid Mechanics Conference*, The University of Sydney, Australia, pp 423-459 (1995).
22. Swanson, R.C. and Turkel, E. "On central difference and upwind scheme", *J. Comp. Phys.*, **101**, pp 297-306 (1992).
23. Baldwin, B.S. and Lomax, H. "Thin-layer approximation and algebraic model for separated turbulent flows", *AIAA Journal*, pp 78-257 (1978).
24. Hartwich, P.M. and Hall, R.M. "Navier-Stokes solutions for vortical flows over a tangent-ogive cylinder", *AIAA Journal*, **28**(7), pp 1171-1179 (1990).
25. Murman, S.M. and Chaderjian, N.M. "Application of turbulence models to separated high-angle-of-attack flows", *AIAA Journal*, pp 98-4519 (Aug. 1998).
26. Landrum, E.J. and Babb, C.D. "Wind-tunnel force, pressure and flow visualization data at Mach numbers from 1.6 to 4.63 for a series of bodies of revolution at angle of attack from -4 to 60 deg", *NASA-TM-X-3558* (Oct. 1977) and *NASA-TM-78813* (March 1979).
27. Levy, Y., Degani, D. and Seginer, A. "Graphical visualization of vortical flows by means of helicity", *AIAA Journal*, **28**(8), pp 1374-1352 (Aug. 1990).